Cloud Detection over Sea Ice Using a Neural Network and Multi-Angle Imaging SpectroRadiometer (MISR) Imagery

Ehsan Mosadegh and Anne W. Nolin

***Abstract*— The Arctic is a cloudy region that often causes satellite images to contain extensive areas of cloud cover. We developed a cloud detection algorithm based on a neural network approach for identifying cloudy and clear pixels over sea ice in Multi-angle Imaging SpectroRadiometer (MISR) images. The training dataset was constructed by using top-of-atmosphere red band values from nine different cameras for two different months, April and July, covering various regions in the Arctic. The labels in the dataset were first visually assessed and divided into training and test datasets with 70% of the dataset used for training and 30% used for independent test data. Model performance was assessed using performance statistics such as Precision, Recall, F score, and Accuracy. The algorithm showed good performance in classifying pixels into cloudy and clear categories in MISR images but results varied by season with better performance for clear pixels in April 2016 and better performance for cloudy pixels in July 2016. This novel algorithm provides a significant advantage over existing MISR cloud mask products. The labeled dataset can be used for further studies cloud detection over sea ice and, with further testing, this method can perhaps be extended to other regions.**

***Index Terms*— neural network, Arctic sea ice, cloud detection and masking, remote sensing, MISR.**

I. INTRODUCTION

Detecting and masking clouds in remotely sensed imagery, particularly over the snow and ice in the polar regions is a challenging task. The difficulty in distinguishing multispectral signatures of snow and cloud leads to uncertainty in cloud detection from satellite data. Cloud detection is crucial for accurate data analysis, given the growing volume of remote sensing images. The unique capability of NASA's Multi-angle Imaging SpectroRadiometer (MISR) to collect angular reflectance information, regardless of spectral details, makes it valuable across fields like climate science, meteorology, and land use planning. Its current cloud mask products aid climate modeling, air quality monitoring, and more.

Three MISR cloud mask products exist, but none is entirely robust for cloud detection, especially over bright surfaces like Arctic ice. The Radiometric Camera-by-Camera Cloud Mask (RCCM) [1] calculates the cloud mask for each of the nine MISR cameras using thresholds based on solar zenith angle, viewing zenith angle, relative azimuth angle, time, and location. The Stereoscopically-Derived Cloud Mask (SDCM) [2] uses a feature image matching technique and stereo observations from multiple MISR cameras to determine whether a pixel is cloudy or clear. The Angular Signature Cloud Mask (ASCM) [1] is based on the Band-Differenced Angular Signature (BDAS) [3] technique and uses blue and near-IR bands in a thresholding technique based on differences between the angular signatures of the two most oblique cameras, Cf and Df. However, no single method appears to be robust for detecting clouds over bright surfaces such as snow and ice in the Arctic. For instance, in the case of detecting clouds over polar regions, RCCM fails to detect clouds effectively over areas with sea ice, and SDCM often fails to detect thin low clouds effectively over polar regions and shows sea ice and water as 'No Retrieval' [4]. Genkova et al (2005) suggested a cloud mask synergy concept for building a consensus cloud mask product for MISR [4]. This concept combines the strength of existing MISR cloud mask products, i.e. RCCM, SDCM, and ASCM. They recommended combining the SDCM and ASCM over snow and ice as the reasonable combination of the existing cloud-mask data products. The consensus algorithm still uses SDCM and ASCM for regions with snow and ice cover and classifies regions into cloudy and clear categories at the spatial resolution of 1.1 km. However, their cloud mask struggles to accurately classify regions with snow and ice cover [4].

In previous work, statistical classifiers have also been used that employed linear correlation matching, quadratic discriminative analysis, and Gaussian kernel support vector machine techniques [5]–[7]. While promising results were obtained in polar cloud classification, these studies utilized only a single MISR path, therefore limiting generalizability.

Of particular interest, a supervised support vector machine (SVM) classifier was developed that used spectral, angular, and texture features to categorize MISR image pixels into various cloudy/clear classes [8]. This approach achieved an approximately 81% global accuracy for cloud classification at a 1.1 km spatial resolution, with an 8% misclassification rate for cloudy pixels over sea ice. The method demonstrated potential for enhanced accuracy by incorporating additional data and optimizing classifier fit for MISR data. It was also extended to train a global-scale cloud classifier using large feature vectors encompassing diverse raw features from

This research was funded on a subcontract (#1623719) through the MISR Project, NASA/Jet Propulsion Laboratory.

Ehsan Mosadegh is with the University of Nevada, Reno, NV 89557, USA. (Email: emosadegh@nevada.unr.edu).

Anne W. Nolin is with the Department of Geography, University of Nevada, Reno, NV 89557, USA. (email: anolin@unr.edu).

different camera angles and spectral bands within a wide spatial neighborhood. The method displayed effectiveness for various global image pixel classification issues, but it was limited to latitudes below 60° in both hemispheres.

In other work, neural networks have been used to construct cloud classification and detection models for various sensors, especially in polar regions [9]–[14]. These approaches departed from traditional threshold-based methods. For example, one method classified MODIS pixels using parameters derived from extensive radiative transfer simulations [15]. It outperformed the MODIS Cloud Mask (MOD35 C6) during winter over snow-covered mid-latitude areas. The technique excelled when applied to SLSTR images for binary cloud classification [16], leveraging inputs like spectral channels, coordinates, zenith angles, and surface-type flags. Similarly, a comparable technique developed a binary cloud classifier for Visible Infrared Imaging Radiometer Suite (VIIRS) images [17]. It employed various channels, a land–water mask, zenith angles, and latitude to outperform existing masks in Greenland.

Other studies explored approaches like combining spectral data with ancillary information [18], SVM for MODIS imagery [19], band-differenced angular signature (BDAS) for MISR imagery [3], [20], rule-based and threshold methods for Sentinel-2 imagery [21], Bayesian techniques for MERIS data [22], spectral, and spatial signature threshold tests for AVHRR [23], and deep convolutional neural networks (CNN) [13], [24], [25], particularly for Landsat 8 imagery [26], [27].

Overall, previous cloud detection algorithms have been shown to have limitations such as poor functionality over snow and ice surfaces, extra calculation steps, and the use of ancillary information. Additionally, cloud masks have only been available at 1.1 km spatial resolution. The goal of this research is to develop an algorithm for MISR images that can detect and mask clouds at a resolution of 275-m, which matches the resolution of our previously-developed sea ice roughness model [28]. Consequently, this study intends to develop a neural network-based binary cloud detection and classification algorithm for MISR images that can provide cloud mask products with a particular focus on the Arctic region.

II. Methodology

The overall approach in developing the cloud detection algorithm was to utilize the angular patterns of reflectance of clouds to differentiate cloudy pixels from clear pixels over sea ice. The algorithm was developed using a machine learning approach trained on cloudy- and clear-sky pixels over two regions in the Arctic for two time periods. The following describes the steps we took to develop the cloud detection algorithm.

MISR is an instrument onboard NASA's Terra satellite. MISR data are available from February 2000 to the present. The instrument has nine push-broom cameras, symmetrically positioned at fixed angles in the forward and aft viewing directions (0°, 23.5°, 60°, 70.5°). The cameras are labeled Da, Ca, Ba, Aa, An, Af, Bf, Cf, Df, where A through D corresponds to 0° through 70.5°, "a" refers to aft-viewing, "f" refers to forward viewing and "n" refers to nadir-viewing. There are 233 geographically distinct MISR orbital paths that provide near-global coverage. The 233 paths repeat every 16 days. Each path is subdivided into 180 blocks, with the block numbers increasing from the north to the south pole. Our study area, north of about 60°N latitude, is covered by MISR blocks 1–46. The An nadir-viewing camera has all four spectral bands and a spatial resolution of 275 m, while for the non-nadir cameras, only the red band is at 275 m resolution; the other bands are spatially aggregated to 1.1 km resolution. Since we wish to distinguish clouds from sea ice based on angular reflectance properties and do so at a spatial resolution that matches our MISR sea ice roughness product, we aim to classify pixels at 275 m spatial resolution and thus use only the red bands. We used the MISR ML1B2-Ellipsoid data product [29] in this research which includes top-of-atmosphere (TOA) radiance measurements. MISR data products in Hierarchical Data Format (HDF) were obtained from the NASA Langley Research Center Atmospheric Science Data Center (ASDC) in Hampton, VA, U.S. We subset the data product to include only the red band radiance information for the nine MISR cameras. At high latitudes, the orbits have some spatial overlap. Thus, MISR observes much of the Arctic every two days. Within each image, data from all nine angles are acquired within a seven-minute window.

We used a subset of MISR images for two 16-day periods to build and label a training dataset and eventually build our cloud binary classifier. Our study area is the Arctic region, north of 60°N latitude. The time frame for selecting sample data covers 16 days (15-30) in April (spring) and 16 days (10-25) in July (summer) 2016. These periods correspond to periods as in [28]. We wanted to develop a training dataset and a cloud binary pixel classifier for our sea ice roughness model and to test the capacity of our developed classifier for detecting and masking cloudy pixels for two 16-day period in spring and summer. The periods are 16 days because that is the exact orbital repeat time for MISR, over which the instrument collects data over all 233 orbital paths. The study area of this research is the Arctic region, north of 60°N (Fig. 1). This region is identical to the study area in our previous work [28] because we developed this cloud mask for our sea ice roughness model.

Fig. 1. Visualization of the study region, north of 60°N. The location of the cloudy block is shown on the map.

To build and label the training and test datasets, we applied our labeling algorithm such that each pixel was labeled with its associated 9 angular reflectance values and a cloud mask value. Each pixel in the dataset has the necessary information such as path, orbit, block, line, and sample numbers to reference that pixel in post-processing steps. The algorithm locates and extracts TOA reflectance values that come from each of the 9 cameras and allocates them to each specific pixel in the training dataset. This method enabled us to collect and build the angular signature from each pixel from 9 cameras. It also finds and extracts the cloud mask values for each pixel from the existing SDCM and ASCM MISR cloud mask products.

Labeling the training dataset for this research entailed two main steps: First, we used cloud classification information from MISR, SDCM, and ASCM cloud masks to label sampled pixels in our training dataset first. We selected these two cloud masks based on Genkova et al (2005) which recommends that the most appropriate combination of masks to use over snow and ice surface types is a combination of SDCM and ASCM. We only selected high-confidence (HC) and low-confidence (LC) labels from SDCM and ASCM products to label our training dataset. Then, in the next step, we assessed every single image pixel in our training dataset visually to confirm pixel labels are correct. For instance, if a pixel label from consensus products was 44 it meant the two products detected that pixel as clear HC. If a pixel label from SDCM and ASCM was 11 it meant the two cloud masks detected that pixel as cloudy HC. Also, if a pixel label from SDCM and ASCM was 41 it meant the SDCM classified that pixel as clear HC (4), but ASCM classified that pixel as cloudy HC (1). When we were visually assessing each pixel in our training dataset, we checked and confirmed if a pixel was actually clear or cloudy with HC or not. Then, two experts performed the subjective cloudy/clear identification on the labeled dataset from the previous step. We reclassified each pixel in our training dataset based on our visual assessment and voting and updated and corrected our training dataset. We performed this step to build our training datasets for both April and July 2016. We used only red band TOA reflectance values from all nine cameras to build our training dataset for each month, April and July. After updating the training datasets with labels from our visual assessment step, we developed our training dataset for April and July 2016. Our visually assessed labels worked as the true value and the basis for comparison for our future accuracy assessment.

Using the labeling algorithm, we built our training dataset with TOA reflectance values the nine red-band cameras at 275-meter resolution. Thus, the input feature vector to our classifier is an array of red band TOA reflectance from nine cameras which forms the angular reflectance signature for a specific pixel. We selected sample pixels from different paths that represented several different locations in the Arctic in both April and July.

To control the quality of the training data, we performed the following steps: For any missing values in a sample pixel, we removed that row with missing data from the training dataset. If any data sample contained negative values, the entire data sample was removed from the training dataset. We removed the whole data sample for a pixel if it had constant and/or zero values and filtered for pixels that had values from all 9 cameras for a single pixel. The final training dataset for each month had the following columns in the dataset: path, orbit, block, line, sample, red-band TOA reflectance values from all 9 cameras, MISR SDCM-ASCM cloud labels, and the visually-assessed and confirmed labels. The data were shuffled and we then assigned 70% of the samples to train and 30% to test the algorithm.

We developed, trained, and tested several neural network architectures for binary classification to identify cloudy and clear pixels in MISR images. We tested different hyperparameters such as the number of layers and the number of nodes per layer to find the best architecture for the model for each season. The best architecture was selected in terms of its performance statistics on independent test data. The neural network model was built using the Keras Sequential API [31]. Details of the final model architecture are presented in the Results section where we also report the performance of the classifier on the test dataset. The algorithm and training datasets were developed using Python programming language and scikit-learn [32] and TensorFlow [33] libraries, which are open-source machine learning libraries for Python.

In our previous study, we found that clouds and cloudy images are likely to contribute to a significant part of the error when developing our sea ice roughness model, i.e., if clouds were present in images that were used to build the training data set for the sea ice roughness model, this would introduce noise to the model results [28]. To reduce uncertainty and noise in training data developed from MISR images and to detect and mask clouds and cloudy pixels in MISR images, we developed our classifier for two classes: cloudy and clear.

After training the algorithm, we assessed the performance of the classifier on the independent test dataset. These were the 30% of the data that were set aside to evaluate the performance of the trained model on unseen new data. We assigned the positive class, e.g., class 1, to the cloudy class, because the cloudy class is the class that is of interest and importance in our study. Therefore, we mapped HC cloudy pixels (11) to 1, and HC clear pixels (44) to 0. We reported the performance of the developed classifier using a confusion matrix and the following set of metrics on independent test datasets for each month, April, and July [34]:

$$\text{Precision} = \frac{\text{TP}}{\text{TP+FP}} \tag{1}$$

$$\text{Recall} = \frac{\text{TP}}{\text{TP+FN}} \tag{2}$$

$$\text{Accuracy} = \frac{\text{TP+TN}}{\text{TP+TN+FP+FN}} \tag{3}$$

$$\text{F} = 2\frac{\text{precision} \times \text{recall}}{\text{precision} + \text{recall}} = \frac{2\,\text{TP}}{2\,\text{TP+FP+FN}} \tag{4}$$

These metrics use True Positive (TP), False Positive (FP), True Negative (TN), and False Negative (FN) to calculate

performance statistics. Precision describes the precision of the classifier in correctly detecting a class, e.g., the proportion of samples that were predicted to be in class 1 (cloudy) and belonged to class 1. Recall describes the proportion of samples that belong to the cloudy class and that were correctly classified by the model. Accuracy is defined as the number of correctly classified samples divided by all samples. F-score is a harmonic mean of Precision and Recall and provides a balance between the two metrics.

III. Results

The training dataset consisted of 2712 pixels for April 2016 and 5802 pixels for July 2016, while the test dataset consisted of 678 pixels and 1451 pixels for April and July, respectively. Samples were selected from 23 MISR paths covering different regions in the Arctic.

We trained the neural network algorithm on the training dataset and examined different architectures and hyperparameters to find the model with the best performance for each season. We eventually selected a fully connected neural network with dense layers as our final model based on classification performance metrics such as Accuracy (see Table II). The algorithm has three dense layers with 64, 32, and 2 neurons, respectively. The input layer has nine inputs. The first two hidden layers use the ReLU activation function [35], while the output layer uses the sigmoid activation function. The model is then compiled with the binary_cross-entropy loss function, the accuracy metric, and the Adam optimizer [35] with a 0.001 learning rate.

Tables I-II list the results of the classification tasks on the test dataset.

TABLE I
CONFUSION MATRIX FOR APRIL AND JULY 2016

Actual classes	Predicted classes		
		Clear	Cloudy
April	Clear	531	4
	Cloudy	56	87
July	Clear	374	102
	Cloudy	37	938

TABLE II
PERFORMANCE STATS FOR APRIL AND JULY 2016

	Class	Precision	Recall	F score
APRIL	0	90%	0.99	0.95
	1	0.96	0.61	0.74
	Accuracy	91%		
JULY	0	91%	0.79	0.84
	1	0.9	0.96	0.93
	Accuracy	90%		

We evaluated the performance of the algorithm for images from two different months, April and July 2016, using confusion matrices and performance statistics. The assessment of the performance of the neural network cloud detector was primarily compared against visual assessment.

Tables I-II show the performance statistics for each season, including Precision, Recall, F score, and Accuracy. We compare the ability of a binary class NN to distinguish between cloudy and clear pixels when given a feature vector containing only TOA reflectance values from the 9 MISR cameras. In a confusion matrix, each row represents a class of true pixels according to expert labels and each column represents the classification decision made by the NN classifier. A perfect classifier, then, would show 100% correct classification down the main diagonal.

The results of the binary classification algorithm for classifying pixels into cloudy and clear in the MISR images are presented in TABLE I. TABLE I shows the confusion matrix for April and July 2016. For April, the classifier correctly predicted 531 clear pixels and 87 cloudy pixels, while misclassifying 56 cloudy pixels as clear and 4 clear pixels as cloudy. For July, the classifier correctly predicted 374 clear pixels and 938 cloudy pixels, while misclassifying 102 clear pixels as cloudy and 37 cloudy pixels as clear.

In April 2016 (Table II), the classifier achieved a Precision of 0.90 for clear pixels and 0.96 for cloudy pixels. The Recall was 0.99 for clear pixels and 0.61 for cloudy pixels. The overall accuracy of the classifier was 91%, and the F score was 0.95 for clear pixels and 0.74 for cloudy pixels. These results indicate that the classifier performed well for clear pixels, with high precision and recall, but had a lower performance for cloudy pixels, particularly in terms of recall.

In July 2016 (Table II), the classifier achieved a Precision of 0.91 for clear pixels and 0.90 for cloudy pixels. The Recall was 0.79 for clear pixels and 0.96 for cloudy pixels. The overall Accuracy of the classifier was 90%, and the F score was 0.84 for clear pixels and 0.93 for cloudy pixels. These results indicate that the classifier performed well for cloudy pixels, with high Precision and Recall, but had a lower performance for clear pixels, particularly in terms of Recall, meaning that it misses identifying some clear pixels in our July dataset.

To illustrate the advantages of our approach, we present an example scene containing clouds here. Fig. 2 is an example of a cloudy scene viewed by MISR from 9 different angles. Fig. 3 shows the cloud masks for the same scene in Fig. 2. We selected 441 pixels from both the NNCM and MISR SDCM-ASCM labels and compared them to our visual assessment, which we took as the true labels of each pixel. We calculated the accuracy metric for this comparison, using only the pixels where both SDCM and ASCM labeled the pixel as either cloudy HC or clear HC. For an unseen block, we randomly selected samples for which we had both visually assessed cloudy/clear labels as well as MISR consensus labels (ASCM and SDCM) available. From these, we calculated the accuracy metric. The reason that the region of the NNCM cloud mask looks smaller than the original images is because a scene on the ground in MISR images shifts from left to right in the MISR image block viewed from DF to DA angles (Fig. 2). We removed pixels that did not have data in all 9 cameras. For example, a pixel from the far-

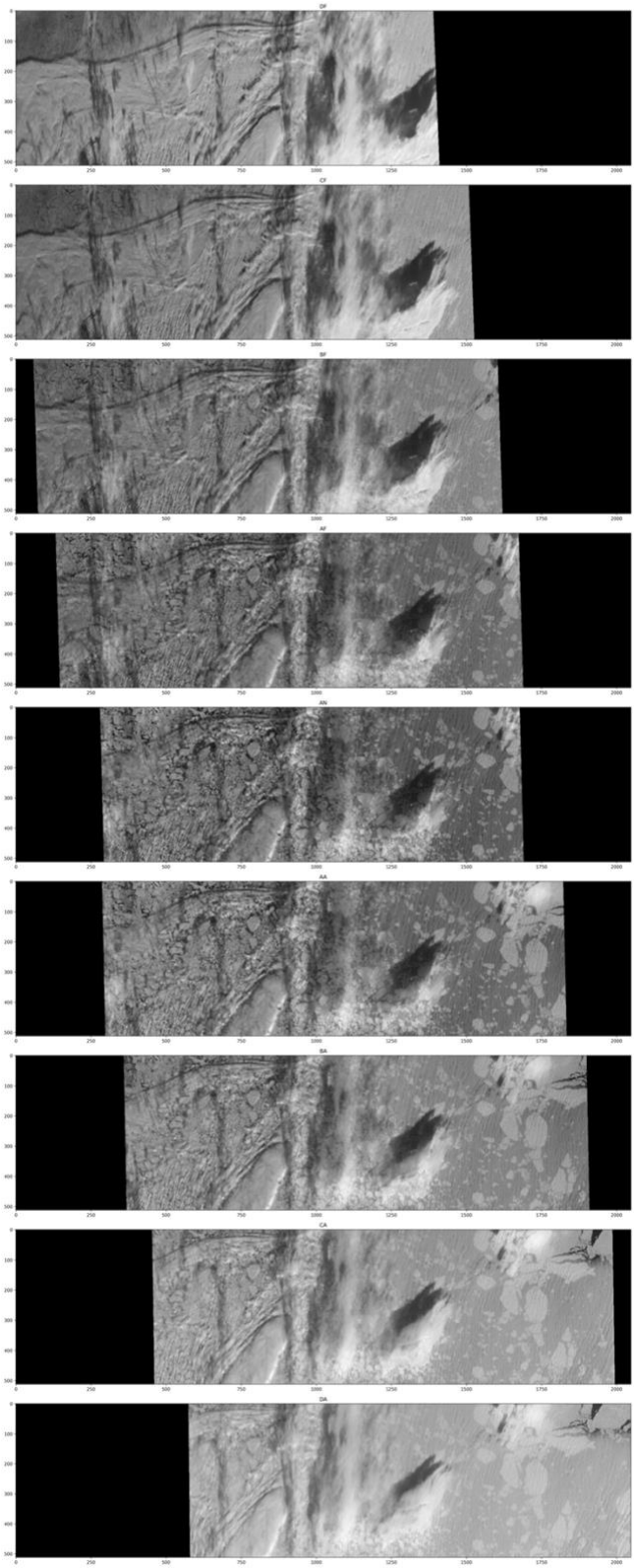

Fig. 2. an example of a cloudy scene viewed by MISR from 9 different angles. This scene is from Block 10, Path 149, Orbit 88247, on July 21, 2016.

left section of an image that has a value in DF might not have a reflectance value in DF. The input features to the NNCM algorithm are reflectance values from all 9 viewing cameras.

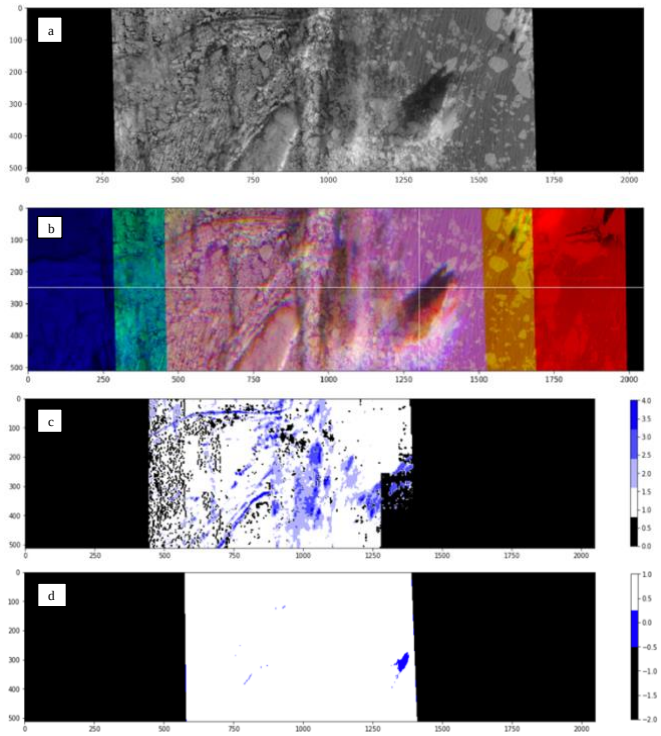

Fig. 3. (a) The grayscale image of a cloudy image from the red band of the An (nadir) camera. (b) A false color composite R(Ca) G(An) B(Cf) image of the same cloudy image. (c) ASCM for the same image. In the ASCM, blue is clear HC, and white is cloudy HC. (d) Visualization of the NNCM for the same image. Blue is clear, and white is cloudy.

These results show that the NNCM can outperform the MISR consensus cloud mask. For the selected image block and sampled pixels, the accuracy of NNCM was 83%, while the accuracy of combined MISR SDCM-ASCM cloud mask products was 1.4%. This indicates a significant improvement in accuracy using our approach compared to the traditional threshold-based methods.

We also calculated the accuracy for SDCM and ASCM labels separately and compared each cloud mask to our visual assessment. For the selected image block and sampled pixels, the accuracy of SDCM was 3.5%, while the accuracy of ASCM was 56%. ASCM had a much better performance compared to SDCM in terms of accuracy based on samples that were taken in this image block. However, compared to ASCM and SDCM, NNCM showed much better performance in terms of accuracy (83%). This indicates that the developed algorithm provides a significant advantage over existing MISR cloud mask products in terms of accuracy and spatial resolution, with a resolution of 275 m.

IV. Discussion and Conclusions

Our neural network-based binary classification algorithm showed good performance in classifying pixels into cloudy and clear categories in MISR images. However, the results showed better performance for clear pixels in April 2016 and better performance for cloudy pixels in July 2016, suggesting areas

for improvement in future iterations of the algorithm.

One of the advantages of our neural network-based approach is that the accuracy is not dependent on threshold values. this makes this approach more flexible to generalize to new and unseen data without recalibration or adjustment of the threshold values for each new image. In contrast, geometry-, threshold- and rule-based techniques such as SDCM, RCCM, or ASCM are often limited by the chosen threshold value, which can lead to incorrect classifications.

Another advantage of our neural network method is that it only uses TOA reflectance values from MISR's nine red cameras as the input to the model. This makes the method parsimonious, efficient, computationally faster compared to models that have more input features, and potentially easier and better at generalizing to new and unseen data. Furthermore, the 275-m resolution of our approach provides a significant advantage over existing 1.1-km MISR cloud mask products.

There are several sources of error in this study. First, the subjective visual assessment and labeling of cloudy and clear pixels could contribute to errors of omission and commission, both of which would influence the Precision, Recall, and F scores. Having two experts performing the subjective cloudy/clear identification helps but is never foolproof. A second source of error is the algorithm itself, which depends on the nature of the training set. The training data set included a range of cloud types (e.g., cirrus, stratus, multiple cloud layers) over various sea ice types (e.g., fast ice, continuous ice cover, fractured ice cover, ice floes) but we could not include all cloud types over all sea ice types. In terms of relative magnitude, we found that false negatives (FN) and false positives (FP) have a similar magnitude of the error. To improve our algorithm, we could consider incorporating additional data sources and refining our labeling and visual assessment methods.

The results of the binary classification algorithm for identifying cloudy and clear pixels in MISR images are promising, but some limitations need to be considered. The algorithm was trained on a dataset for only two months, April and July 2016, and samples were selected from different MISR paths covering different regions in the Arctic. This could limit the algorithm's generalizability to other months or regions. While we selected samples from 12 MISR paths, which covered different regions in the Arctic, the analysis was not spatially comprehensive. However, we also combined both training datasets for April and July and trained a model with that combined training dataset and we noticed the accuracy of the model decreased although not significantly compared to the accuracy for every single dataset.

Another potential limitation is that the current algorithm only distinguishes between cloudy and clear pixels and does not provide cloud detection confidence estimates, which is a limitation compared to SDCM and ASCM which differentiate between more classes (cloud high confidence, cloud low confidence, clear low confidence, and clear high confidence). Additionally, our algorithm struggles to distinguish cloud shadows and thin clouds. We note that this is difficult even for experts when visually trying to assess and evaluate a scene using RGB composite images.

In conclusion, the binary cloud classification algorithm developed in this study is highly promising for cloud detection in MISR images over sea ice. This algorithm could be further refined and extended to the Antarctic. It would also be valuable to test this algorithm over the full timeframe of MISR data collection (2000-present) to create a cloud classification product to accompany the sea ice roughness algorithm that was developed by [28].

Results from this study point to the need for additional classes such as thin clouds and cloud shadows. This will require more training data samples and a more robust visual assessment of data. Future research should explore the potential of combining the developed algorithm with other approaches, such as multispectral and multitemporal analyses, to improve the accuracy of cloud detection in MISR images for different categories and classes such as thin clouds and cloud shadows. Moreover, with a global training data set this machine learning approach could be generalized to create a global cloud detection algorithm. The development of accurate cloud detection algorithms is crucial for improving our understanding of the Earth's climate and the impacts of climate change.

ACKNOWLEDGMENT

This work was supported by NASA/Jet Propulsion Laboratory Contract #1623719. Image data were obtained from the NASA Langley Research Center Atmospheric Science Data Center.

REFERENCES

[1] D. J. Diner, L. Di Girolamo, and E. E. Clothiaux, "MISR Level 1 Cloud Detection Algorithm Theoretical Basis." JPL Internal Docs. D-13397, Rev. B, Dec. 1999. [Online]. Available: [Available from JPL Documentation Services, 4800 Oak Grove Dr., Pasadena, CA 91109.]

[2] D. J. Diner *et al.*, "MISR Level 2 Cloud Detection and Classification Algorithm Theoretical Basis," JPL Pasadena, CA, JPL Internal Doc. D-11399, Rev. C, 1997, Dec. 1999. [Online]. Available: [Available from JPL Documentation Services, 4800 Oak Grove Dr., Pasadena, CA 91109.]

[3] L. Di Girolamo and M. J. Wilson, "A first look at band-differenced angular signatures for cloud detection from MISR," *IEEE Trans. Geosci. Remote Sens.*, vol. 41, no. 7, pp. 1730–1734, Jul. 2003, doi: 10.1109/TGRS.2003.815659.

[4] I. Genkova *et al.*, "The synergy of the MISR cloud masks for global cloud climatology," *Proc SPIE*, Oct. 2005, doi: 10.1117/12.627909.

[5] T. Shi, B. Yu, E. E. Clothiaux, and A. J. Braverman, "Daytime Arctic Cloud Detection Based on Multi-Angle Satellite Data with Case Studies," *J. Am. Stat. Assoc.*, vol. 103, no. 482, pp. 584–593, 2008.

[6] T. Shi, E. E. Clothiaux, B. Yu, A. J. Braverman, and D. N. Groff, "Detection of daytime arctic clouds using MISR and MODIS data," *Remote Sens. Environ.*, vol. 107, no. 1–2, pp. 172–184, Mar. 2007, doi: 10.1016/j.rse.2006.10.015.

[7] T. Shi, B. Yu, E. E. Clothiaux, and A. J. Braverman, "Cloud Detection over Snow and Ice Using MISR Data," p. 27.

[8] D. Mazzoni, M. J. Garay, R. Davies, and D. Nelson, "An operational MISR pixel classifier using support vector machines," *Remote Sens. Environ.*, vol. 107, no. 1–2, pp. 149–158, Mar. 2007, doi: 10.1016/j.rse.2006.06.021.

[9] S. Larosa *et al.*, "A Cloud Detection Neural Network Approach for the Next Generation Microwave Sounder Aboard EPS MetOp-SG A1," *Remote Sens.*, vol. 15, no. 7, Art. no. 7, Jan. 2023, doi: 10.3390/rs15071798.

[10] V. Afzali Gorooh *et al.*, "Deep Neural Network Cloud-Type Classification (DeepCTC) Model and Its Application in Evaluating

PERSIANN-CCS," *Remote Sens.*, vol. 12, no. 2, Art. no. 2, Jan. 2020, doi: 10.3390/rs12020316.
[11] Y. Jiang *et al.*, "A Cloud Classification Method Based on a Convolutional Neural Network for FY-4A Satellites," *Remote Sens.*, vol. 14, no. 10, Art. no. 10, Jan. 2022, doi: 10.3390/rs14102314.
[12] X. Li, X. Yang, X. Li, S. Lu, Y. Ye, and Y. Ban, "GCDB-UNet: A novel robust cloud detection approach for remote sensing images," *Knowl.-Based Syst.*, vol. 238, p. 107890, Feb. 2022, doi: 10.1016/j.knosys.2021.107890.
[13] Z. Shao, Y. Pan, C. Diao, and J. Cai, "Cloud Detection in Remote Sensing Images Based on Multiscale Features-Convolutional Neural Network," *IEEE Trans. Geosci. Remote Sens.*, vol. 57, no. 6, pp. 4062–4076, Jun. 2019, doi: 10.1109/TGRS.2018.2889677.
[14] S. Pang, L. Sun, Y. Tian, Y. Ma, and J. Wei, "Convolutional Neural Network-Driven Improvements in Global Cloud Detection for Landsat 8 and Transfer Learning on Sentinel-2 Imagery," *Remote Sens.*, vol. 15, no. 6, Art. no. 6, Jan. 2023, doi: 10.3390/rs15061706.
[15] N. Chen *et al.*, "New neural network cloud mask algorithm based on radiative transfer simulations," *Remote Sens. Environ.*, vol. 219, pp. 62–71, Dec. 2018, doi: 10.1016/j.rse.2018.09.029.
[16] C. Poulsen, U. Egede, D. Robbins, B. Sandeford, K. Tazi, and T. Zhu, "Evaluation and comparison of a machine learning cloud identification algorithm for the SLSTR in polar regions," *Remote Sens. Environ.*, vol. 248, p. 111999, Oct. 2020, doi: 10.1016/j.rse.2020.111999.
[17] C. H. White, A. K. Heidinger, and S. A. Ackerman, "Evaluation of Visible Infrared Imaging Radiometer Suite (VIIRS) neural network cloud detection against current operational cloud masks," *Atmospheric Meas. Tech.*, vol. 14, no. 5, pp. 3371–3394, May 2021, doi: 10.5194/amt-14-3371-2021.
[18] G. Riggs and D. K. Hall, "Reduction of Cloud Obscuration in the MODIS Snow Data Product," presented at the 59th EASTERN SNOW CONFERENCE, Stowe, Vermont USA: EASTERN SNOW CONFERENCE, Jan. 2002.
[19] R. Zhang, D. Sun, S. Li, and Y. Yu, "A stepwise cloud shadow detection approach combining geometry determination and SVM classification for MODIS data," *Int. J. Remote Sens.*, vol. 34, no. 1, pp. 211–226, Jan. 2013, doi: 10.1080/01431161.2012.712231.
[20] L. Di Girolamo and R. Davies, "A band-differenced angular signature technique for cirrus cloud detection," *IEEE Trans. Geosci. Remote Sens.*, vol. 32, no. 4, pp. 890–896, Jul. 1994, doi: 10.1109/36.298017.
[21] V. Zekoll *et al.*, "Comparison of Masking Algorithms for Sentinel-2 Imagery," *Remote Sens.*, vol. 13, no. 1, Art. no. 1, Jan. 2021, doi: 10.3390/rs13010137.
[22] L. Istomina, H. Marks, M. Huntemann, G. Heygster, and G. Spreen, "Improved cloud detection over sea ice and snow during Arctic summer using MERIS data," *Atmospheric Meas. Tech.*, vol. 13, no. 12, pp. 6459–6472, Dec. 2020, doi: 10.5194/amt-13-6459-2020.
[23] L. L. Stowe, P. A. Davis, and E. P. McClain, "Scientific Basis and Initial Evaluation of the CLAVR-1 Global Clear/Cloud Classification Algorithm for the Advanced Very High Resolution Radiometer," *J. Atmospheric Ocean. Technol.*, vol. 16, no. 6, pp. 656–681, Jun. 1999, doi: 10.1175/1520-0426(1999)016<0656:SBAIEO>2.0.CO;2.
[24] J. Guo, J. Yang, H. Yue, H. Tan, C. Hou, and K. Li, "CDnetV2: CNN-Based Cloud Detection for Remote Sensing Imagery With Cloud-Snow Coexistence," *IEEE Trans. Geosci. Remote Sens.*, vol. 59, no. 1, pp. 700–713, Jan. 2021, doi: 10.1109/TGRS.2020.2991398.
[25] Q. He, X. Sun, Z. Yan, and K. Fu, "DABNet: Deformable Contextual and Boundary-Weighted Network for Cloud Detection in Remote Sensing Images," *IEEE Trans. Geosci. Remote Sens.*, vol. 60, pp. 1–16, 2022, doi: 10.1109/TGRS.2020.3045474.
[26] M. J. Hughes and R. Kennedy, "High-Quality Cloud Masking of Landsat 8 Imagery Using Convolutional Neural Networks," *Remote Sens.*, vol. 11, no. 21, Art. no. 21, Jan. 2019, doi: 10.3390/rs11212591.
[27] S. Ji, P. Dai, M. Lu, and Y. Zhang, "Simultaneous Cloud Detection and Removal From Bitemporal Remote Sensing Images Using Cascade Convolutional Neural Networks," *IEEE Trans. Geosci. Remote Sens.*, vol. 59, no. 1, pp. 732–748, Jan. 2021, doi: 10.1109/TGRS.2020.2994349.
[28] E. Mosadegh and A. W. Nolin, "A New Data Processing System for Generating Sea Ice Surface Roughness Products from the Multi-Angle Imaging SpectroRadiometer (MISR) Imagery," *Remote Sens.*, vol. 14, no. 19, Art. no. 19, Jan. 2022, doi: 10.3390/rs14194979.
[29] D. J. Diner, "MISR Level 1B2 Ellipsoid Data (MI1B2E_V1)." Aug. 24, 2013. Accessed: Apr. 24, 2023. [Online]. Available: https://ntrs.nasa.gov/citations/20080012163
[30] E. Mosadegh, "A New Data Processing System for Generating Sea Ice Surface Roughness and Cloud Mask Data Products From the Multi-Angle Imaging SpectroRadiometer (MISR)," Ph.D. dissertation, University of Nevada, Reno, United States -- Nevada, 2023. Accessed: Aug. 16, 2023. [Online]. Available: https://www.proquest.com/docview/2830108213/abstract/6B16832FD9634F5APQ/1
[31] "Keras: The high-level API for TensorFlow | TensorFlow Core," *TensorFlow*. https://www.tensorflow.org/guide/keras (accessed Aug. 27, 2023).
[32] L. Buitinck *et al.*, "API design for machine learning software: experiences from the scikit-learn project," *arXiv.org*, Sep. 01, 2013. https://arxiv.org/abs/1309.0238v1 (accessed Aug. 27, 2023).
[33] M. Abadi *et al.*, "TensorFlow: Large-Scale Machine Learning on Heterogeneous Distributed Systems".
[34] D. L. Olson and D. Delen, "Advanced Data Mining Techniques," *Springer Berl. Heidelb.*, 2008, doi: https://doi.org/10.1007/978-3-540-76917-0.
[35] I. J. Goodfellow, Y. Bengio, and A. Courville, *Deep Learning*. MIT Press, 2016.

Ehsan Mosadegh received the B.S. degree in Civil Engineering from Azad University in Mashhad, Iran in 2009, the M.S. degree in Air Pollution Engineering from the University of Tehran, Iran, in 2013, and the M.S. and Ph.D. degrees in atmospheric sciences from the University of Nevada, Reno, in 2022 and 2023, respectively.

His primary research interests lie in utilizing machine learning and data analysis techniques to address critical environmental challenges.

He is a member of the American Geophysical Union.

Anne W. Nolin received the B.A. degree in anthropology and the M.S. degree in soils, water, and engineering from the University of Arizona, Tucson, in 1980 and 1987, respectively. She received the Ph.D. degree in geography from the University of California, Santa Barbara, in 1993.

Since 2018, she has been a professor in the Department of Geography at the University of Nevada, Reno. Previously, she was a professor at Oregon State University (2003-2018) and a Research Scientist at the University of Colorado, Boulder (1993-2002). Her research integrates studies of cryosphere and climate with innovative methods of satellite observations.

She is a member of the MISR Science Team and the American Geophysical Union.